An analytical model for oblique wave interaction with a partially reflective harbor structure

María L. Jalón[a], Andrea Lira-Loarca[b,*], Asunción Baquerizo[b], Miguel Ángel Losada[b]

[a] *Naval Architecture, Ocean and Marine Engineering, University of Strathclyde. 100 Montrose St, G4 0LZ Glasgow, United Kingdom.*
[b] *Andalusian Institute for Earth System Research. University of Granada. Avda. del Mediterráneo s/n, 18006 Granada, Spain.*

Abstract

An analytical model of the interaction of oblique incident regular waves with a maritime structure is developed and extended to irregular waves. The structure is composed of a semi-submergible vertical impermeable plate enclosing a chamber. Linear wave theory is considered, taking into account the head loss due to the constriction of the flow. The results are compared to those obtained with computational fluid dynamics models, revealing that the proposed model is capable to efficiently describe the performance of these systems for weakly non-linear incident waves. The influence of fundamental design parameters, such as geometric and wave characteristics, on the hydrodynamic behavior and the loadings on the plate is analyzed.

When dealing with irregular waves, the spectra at the seaward region and inside the chamber show a nodal and antinodal structure that varies with the distance to the reflector. This structure, as well as the phase lag between the free surface elevations at both sides of the plate, affect the total loads over the plate. The statistical analysis of the free surface elevation, wave heights, and crests and throughs of the forces is also presented to evaluate the effect of the geometry in both regions and over the plate.

The results show that the model allows to efficiently test different configurations to control wave reflection at the structure and the oscillation in the chamber. It can therefore be applied e.g. for the optimization of the design towards (i) harbor tranquility in the seaward region, (ii) energy extraction inside the chamber and (iii) loads on the structure.

As an application, a failure mode defined as the excess of a critical predefined load over the plate, is analyzed by means of Monte Carlo simulations using known theoretical distributions fitted to the random variables. The results show the importance of the analysis of the performance of the system regarding not only the effect inside the chamber but also on the structure.

Keywords: Analytical model, Oblique waves, Head loss, Harbor tranquility, Optimization

*Corresponding author.
aliraloarca@ugr.es

1. Introduction

The modeling of the wave-structure interactions is a challenging problem with important applications in coastal engineering (Goda, 2010; Sawaragi, 1995). Such is the case of energy dissipation structures, with more research being carried out towards an optimization of the design in regard to the space limitations and the need to control wave reflection and incident sea wave dissipation (Faraci et al., 2015; Liu and Faraci, 2014). On the other hand, the rapid development of wave energy extraction devices has increased the research on the combination of breakwaters with power generation structures (Mustapa et al., 2017) where the complexity of the interactions taking place leads to the adoption of complex numerical codes. However, these codes are not practical during the decision-making or predesign phase of the project, given their computational cost. Therefore, the use of accurate analytical models is essential to assess the optimal parameters of the systems on the first stages of design (Liu and Li, 2013; Monk et al., 2013).

The hydrodynamic behavior of marine structures using analytical models has been analyzed in different research studies. In general, these models consider the velocity potential problem and the solution based on the method of eigenfunction expansion. The differences between the studies found in literature, reside in the wave type and matching conditions.

For example, the modeling of vertical thin barriers as breakwaters using an analytical model was studied by Losada et al. (1992, 1993b). Other type of energy dissipation structures are perforated/slotted walls, in which it is necessary to consider the energy dissipation mechanism in the matching conditions. This is the case of a Jarlan-type breakwater that consists of a perforated front wall and a vertical impermeable back wall (Jarlan, 1961). Bennett et al. (1992) developed a theory for calculating the reflection coefficient based on the study of energy dissipation by Mei (1989); Mei et al. (1974) using a semi-empirical description of the eddy-shedding at the perforated wall for such structures. Isaacson et al. (1998) analyzed the wave interactions with a thin vertical slotted barrier, taking into account the energy dissipation according to Sollitt and Cross (1972). More recently, Liu et al. (2007) analyzed an infinite array of partially perforated caissons with transverse sidewalls following the work by Yu (1995) to define the boundary conditions along the perforated front walls. They obtained the values of the main influencing factors for which the hydrodynamic performance was optimum.

Isaacson et al. (2000) considered a rock-filled core between the slotted wall and the impermeable wall, to increase the dissipation inside the wave-absorbing chamber. The energy dissipation through the slotted wall was considered following Yu (1995), and the effect of the rock fill was accounted for by modifying the free surface boundary condition (Dalrymple et al., 1991). They found that the rock fill could increase wave reflection and reduce wave forces on the system. Liu and Faraci (2014) suggested a variant of this system, in which the rock fill had a slope and the slotted wall was replaced by a rigid vertical barrier with an open window. A semi-analytical solution for normal incidence was proposed and validated using the results from

physical model tests (Faraci et al., 2012), obtaining an excellent agreement between the two models. These type of structures have a versatile character and can be aimed at protecting a harbor or as wave energy converters as studied by Boccotti (2012); Falcão (2000); Torre-Enciso et al. (2009).

In this paper we present an efficient analytical tool to search for an optimal configuration concerning different design criteria such as harbor tranquility, wave energy extraction and structural safety that usually implies a trade-off between performance and structural design. We analyze the interaction of obliquely incident wave trains with a chamber delimited by a thin vertical semi-immersed barrier and an impermeable back wall. These models are computationally efficient and allow the analysis and optimization of the systems at a predesign stage (Jalón et al., 2016; Lovas et al., 2010; Martins-Rivas and Mei, 2009).

The theoretical formulation is based on linear theory and takes into account the angle of incidence and the momentum loss due to the constriction of the flow (Mei et al., 1974). Its performance is compared with the results obtained with a numerical model.

More precisely, we analyzed the influence of fundamental aspects of the design, such as the structure's geometric parameters and wave characteristics on the wave patterns in the regions divided by the barrier. It is found that the phase lag between the wave trains at both sides of the plate and the nodal and antinodal structure of the frequency spectrum of the oscillation in the seaward region play a key role in the tranquility seawards, the amplification/attenuation of the oscillation inside the chamber and in the total loads on the plate. This result is key towards an optimal design of the structure and it shows that the design should be based not only on the geometry or wave characteristics but also on the energy transmission at both sides of the plate.

The paper is organized in seven sections. After the introduction, the theoretical formulation is presented. Section 3 presents the analysis of the hydrodynamic performance for regular waves. Section 4 depicts the extension of the model to irregular waves. In section 5 we present and analyze the results for regular and irregular waves. Section 6 presents an application of the methodology using simulation techniques for uncertainty assessment. Finally, the main conclusions are included in section 7.

2. Theoretical formulation

We consider the interaction of a monochromatic wave train with a marine structure that consists of a fixed vertical barrier of thin thickness and infinite width, submerged a depth d and spaced a distance B from a vertical and solid back wall on a horizontal bed (Figure 1). The origin of the cartesian system is located at the plate lying over the still water level (SWL). The x-axis points to the wall, the y-axis lies along the plate and the z-axis points upwards. The incident wave, with amplitude A_0 and angular frequency ω is assumed to impinge obliquely on the barrier, propagating at an angle θ measured from the positive direction of the x-axis. For the sake of simplicity the barrier is assumed to have an infinite width (y-axis).

Assuming irrotational flow and incompressible and non-viscous fluid, the problem may be formulated in terms of the velocity potential which satisfies the Laplace equation in the fluid, the kinematic conditions at the boundaries and the mixed boundary condition on the free surface. The barrier divides the domain into a seaward region ($x < 0$) and a leeward region with velocity potentials Φ_1 and Φ_2 respectively. The velocity potentials Φ_n $(n = 1, 2)$ can be expressed as,

$$\Phi_n(x, y, z, t) = \Re\{\phi_n(x, z)e^{i(\lambda y - \omega t)}\} \tag{1}$$

where $\Re\{.\}$ refers to the real part, t is time, and $\lambda = k_0 \sin\theta$ with k_0 being the incident wavenumber corresponding to the real solution k of the dispersion equation,

$$\frac{\omega^2}{g} = k \tanh(kh) \tag{2}$$

The velocity potential Φ_n, results from the superposition of a partial standing plane wave and a series of evanescent modes (Losada et al., 1993a) that decay far from the obstacle. These terms correspond to the eigenfunctions of the problem in z that arise from separation of variables and that are associated to the pure imaginary roots ($k_l = ik'_l$, $l = 1, 2, ...$ with k'_l a positive real number) of the dispersion equation. Their expressions are given by:

$$\begin{aligned} \phi_1(x, z) &= A_0 I_0(z) e^{i\Gamma_0 x} + \sum_{l=0}^{\infty} D_l I_l(z)\, e^{-i\Gamma_l x} \qquad \text{for } x < 0 \\ \phi_2(x, z) &= \sum_{l=0}^{\infty} C_l I_l(z) \left(e^{i\Gamma_l x} + e^{-i\Gamma_l (x-2B)}\right) \quad \text{for } 0 < x < B \end{aligned} \tag{3}$$

where,

$$I_l(z) = \frac{-ig}{\omega} \frac{\cosh(k_l(h + z))}{\cosh(k_l h)} \tag{4}$$

$$\Gamma_l = \sqrt{k_l^2 - \lambda^2} \tag{5}$$

In Equation 3 I_0 and Γ_0 represent, respectively, the depth dependent function and the component in the x-direction of the wavenumber vector of the propagating modes of the incident and reflected wave trains ($\Gamma_0 = k_0 \cos\theta$). In the seaward region, the complex amplitude of the reflected wave is D_0 and the amplitudes of the evanescent modes are D_l $(l > 0)$. Inside the chamber, the solution consists of the complex amplitude of the propagating mode C_0 and a set of evanescent modes with coefficients C_l $(l > 0)$. These modes contain the terms that decay far from the plate and far from the wall respectively. This velocity potential Φ_2 already meets the non-flux condition at the wall ($x = B$).

Since the solutions at both regions must match at their common interface, the velocity potentials must satisfy the following conditions:

(a) Horizontal velocities are equal in the gap.

(b) There is no flow through the plate.

(c) Surface elevations at both sides of the plate differ in a momentum loss term.

The momentum loss is formulated following the model of quadratic head loss by Mei et al. (1974):

$$\eta_1(x,z,t) - \eta_2(x,z,t) = \frac{f}{2g} u_2(x,z,t)|u_2(x,z,t)| + \frac{\Upsilon_i}{g}\frac{\partial u_2(x,z,t)}{\partial t} \tag{6}$$

where u_2 is the horizontal velocity at the gap, f is the friction coefficient that depends primarily on the gap geometry, and Υ_i is an inertia coefficient that may be determined empirically. Equation (6) is obtained from the momentum balance and the continuity equation in a control volume centered at the plate. The terms in the left-hand side are, therefore, proportional to the pressure terms in the Bernoulli equation. The first term in the right-hand side arises from the convective terms while the second one is related to the local acceleration and is small compared to the former. This model has been successfully applied to other related problems (Baquerizo et al., 2002; Roldán et al., 1992).

In this work an empirical expression for f that is valid for sharp-edged orifices (Mei et al., 2005) is used:

$$f = \left(\frac{1}{C\epsilon} - 1\right)^2 \tag{7}$$

where $C = 0.6 + 0.4\epsilon^3$ and $\epsilon = \frac{h-d}{h}$ is the relative aperture.

The friction term can be linearized by introducing an equivalent friction coefficient C_e which depends on the velocity at the gap u_2. The linearized term is then required to give the same energy loss per period than the quadratic one. An error e introduced by the linearization process can be defined as follows:

$$e = \frac{f}{2g} u_2|u_2| - C_e u_2 \tag{8}$$

C_e is chosen so that the mean square of the error is minumum. Following Mei et al. (2005), time-averaging e^2 gives,

$$\overline{e^2} = \overline{\left(\frac{f}{2g} u_2|u_2|\right)^2} - \frac{f}{g} C_e \overline{u_2^2|u_2|} + C_e^2 \overline{u_2^2} \tag{9}$$

where the overbar indicates the average over one wave period.

The minimum value of Equation 9 is found by equating $\frac{\partial \overline{e^2}}{\partial C_e} = 0$ to zero and by approximating u_2 by a simple harmonic, which leads to the following expression for C_e:

$$C_e(x,z) = \frac{4f}{3\pi}|u_2(x,z)| \tag{10}$$

In Equation 10, $|u_2(x,z)| \approx |C_0 I_0(z) i\Gamma_0 (e^{i\Gamma_0 x} - e^{-i\Gamma_0(x-2B)})|$ obtained from the velocity potential ϕ.

C_e depends on the amplitude of the oscillation and, given that u_2 varies with depth, it also depends on the coordinate z. Finally, the matching conditions at the plate, $x = 0$, are:

$$\frac{\partial \phi_1}{\partial x} = \frac{\partial \phi_2}{\partial x} \qquad -h < z < -d \tag{11a}$$

$$\frac{\partial \phi_1}{\partial x} = \frac{\partial \phi_2}{\partial x} = 0 \qquad -d < z < 0 \tag{11b}$$

$$\phi_1(x,z) - \phi_2(x,z) = -\frac{i}{\omega} C_e(x,z)\phi_{2,x}(x,z) \qquad -h < z < -d \tag{11c}$$

Following Losada et al. (1992) and making use of the fact that $\{I_l(z)\}_{l=1}^{\infty}$ is a set of orthogonal functions, it is shown that the condition of equal velocities at the gap is met if $D_l = A_0 - C_l(1 - e^{i2B\Gamma_l})$, $l = 0$ and $D_l = -C_l(1 - e^{i2B\Gamma_l})$, $l > 0$. In order to simultaneously solve the other two matching conditions related to the impermeability of the plate and the head loss at the gap, their left hand terms are truncated to N_l terms and combined into the following piecewise function $G(z)$:

$$G(z) = \begin{cases} -2A_0 I_0(z) + \sum_{l=0}^{N_l} C_l I_l(z) \left[2 + \Gamma_l \frac{C_e}{\omega}(1 - e^{i2B\Gamma_l})\right] & \text{for } -h < z < -d \\ \sum_{l=0}^{N_l} C_l I_l(z) i\Gamma_l \left(1 - e^{i2B\Gamma_l}\right) & \text{for } -d < z < 0 \end{cases} \tag{12}$$

To ensure that the modulus of the complex function $G(z)$ is almost zero, the coefficients C_l that minimize the following integral are searched:

$$\int_{-h}^{0} |G(z)|^2 dz \tag{13}$$

Equation (13) leads to the following set of equations:

$$\int_{-h}^{0} G(z)^* \frac{\partial G(z)}{\partial C_m} dz = 0 \quad \text{for } m = 0, 1, ..., N_l \tag{14}$$

where * indicates the complex conjugate.

An iterative procedure is required to solve the problem (Equation 14) given that $C_e(z)$ depends on the amplitude of the horizontal velocity $|u_2(x = 0, z)|$ and that this is an unknown variable of the problem.

3. Hydrodynamic performance

Once the C_l coefficients have been obtained, the kinematic and dynamic properties of interest can be derived from the velocity potential.

The equations for the free surface elevation in each region are:

$$\begin{aligned} \eta_1(x,y,t) &= \Re\left\{\left[A_0(e^{i\Gamma_0 x} + e^{-i\Gamma_0 x}) - \sum_{l=0}^{N_l} C_l(1 - e^{i2B\Gamma_l})e^{-i\Gamma_l x}\right] e^{i(\lambda y - \omega t)}\right\} \qquad \text{for } x < 0 \\ \eta_2(x,y,t) &= \Re\left\{\sum_{l=0}^{N_l} C_l \left(e^{i\Gamma_l x} + e^{-i\Gamma_l (x-2B)}\right) e^{i(\lambda y - \omega t)}\right\} \qquad \text{for } 0 < x < B \end{aligned} \tag{15}$$

The complex reflection coefficient in region 1 and the complex capture coefficient in region 2 can be derived with respect to incident wave amplitude A_0 and the complex amplitude C_0 of the propagating wave inside the chamber, for the reflected and captured waves.

The modulus of the reflection coefficient, K_R, is,

$$K_R = \frac{|A_0 - C_0(1 - e^{i2B\Gamma_0})|}{|A_0|} \tag{16}$$

The modulus of the capture coefficient, K_C, is defined as,

$$K_C = \frac{|C_0|}{|A_0|} \tag{17}$$

An amplification factor Q is defined as the ratio between the mean wave amplitude inside the chamber and the incident wave amplitude:

$$Q = \frac{1}{B|A_0|} \int_0^B |\eta_2| dx \tag{18}$$

and the phase lag is $\Psi = \omega t_{max}$ with t_{max} being the time difference of the maximum surface elevation occurrences at $x = 0$.

The pressure field associated with the surface elevation in each region can be expressed as:

$$P_k(z,t) = \begin{cases} \rho_\omega g \left(\frac{cosh(k(h+z))}{cosh(kh)} \eta_k - z \right) & z \leq 0 \\ \rho_\omega g \left(\eta_k - z \right) & z > 0 \end{cases} \qquad k = 1, 2 \tag{19}$$

where η_k is the water surface displacement at the plate on each region and ρ_ω is the density of water. The instantaneous force exerted on the plate can be calculated by integrating the pressure over depth per unit width of plate:

$$F_t(t) = F_1(t) - F_2(t) = \int_{-d}^{\eta_1} P_1(z,t) dz - \int_{-d}^{\eta_2} P_2(z,t) dz \tag{20}$$

The positive values of the total force ($F_1 > F_2$) correspond to leeward-acting forces F_l (forces exerted towards the chamber) and the negative values ($F_2 > F_1$) correspond to seaward-acting forces F_s. Therefore, the peak forces are obtained as the maximum and minimum values of the total force in a wave period T and correlate to the maximum values of the leeward-acting and seaward-acting forces. It is worth mentioning that the equilibrium requirements involve the calculation of not only the forces but also the moments acting on the structure in each direction. In this case, we have focused only on the forces as an intuitive and simple variable to analyze the hydrodynamics of the system under different wave and geometrical conditions.

4. Extension to irregular waves

Ocean waves are random in nature. There are several ways to calculate the characteristics of the hydrodynamics for irregular waves using regular wave models (Huang et al., 2011). For the system under consideration, based on the fact that linear wave theory has been used, we can assume the irregular sea state to be the result of the superposition of a number of harmonic components with potential functions $\Phi_{m,j}$ that satisfy the governing equations, the boundary conditions and the matching conditions at the common interface as explained in sections 2-3. In order to obtain a feasible realization of the irregular wave train, for a given incident spectrum $S(\omega)$, we divide the range of angular frequencies of interest into N_j bands $(\omega_{j-1}, \omega_j], j = 1, ..., N_j$ of equal width $\Delta\omega = \omega_j - \omega_{j-1}$.

$$\Phi_m(x, y, z, t) = \sum_{j=1}^{N_j} \Phi_{m,j}(x, y, z, t) = \Re\left\{ \sum_{j=1}^{N_j} \phi_{m,j}(x, z) e^{i(\lambda_j y - \omega_j t)} \right\} \quad m = 1, 2 \tag{21}$$

Therefore, the incident irregular wave train is the superposition of regular wave components of angular frequencies ω_j and complex amplitudes A_0^j given by

$$A_0^j = |A_0^j| e^{i\varphi_j} = \sqrt{2S(\omega_j)\Delta\omega_j} e^{i\varphi_j}, \quad j = 1, 2, ..., N_j \tag{22}$$

where the phases φ_j are randomly obtained from a uniform distribution over $[0, 2\pi]$.

It is assumed that the incident wave energy is distributed in a range of frequencies (ω_L, ω_H) therefore neglecting a percentage of energy in the lowest and highest frequencies (Liu et al., 2008). The corresponding surface elevation and wave forces time series for each region can be obtained by solving the equations of sections 2-3 for each component.

5. Results

5.1. Model comparison

The goodness of the model presented in this work was verified by means of (1) the degree of fulfillment of the boundary conditions and (2) the comparison of results with Fluent and Fluinco, two widely accepted computational fluid dynamics models.

Firstly, the model was run for different values of the number of evanescent modes, N_l, to analyze the order of magnitude for the error of the calculations when truncating the series for intermediate water depths. The calculations shown as examples in Figures 3 and 4 were obtained for $h = 10.0$ m, $d/h = 0.5$, $B/h = 1$ and a normal incident wave with $A_0 = 0.5$ m and $kh = 1.717$.

Figure 3 represents the horizontal velocity component $|u|$ at $x = 0$ and $z = 0$ on the seaward face of the plate, where the impermeability condition is imposed. As observed, the solution converges as N_l increases and the order of magnitude for the error is $\approx O(10^{-2})$ for $N_l \geq 50$ and under $O(10^{-3})$ for $N_l \geq 200$.

Therefore, unless otherwise stated, all the results presented henceforth are calculated for $N_l = 200$. Other values selected for the analysis are $A_0 = 0.5$ m and $h = 10.0$ m.

In order to illustrate that the agreement of the model is not only local but uniform in z, the depth dependent function $G(z)$, that measures the goodness of the fulfillment of the boundary conditions, is represented in Figure 4 for different values of relative width B/L with L being the wavelength at the front of the structure for a depth h ($L = 2\pi/k_0$). According to its definition, $G(z)$ should be approximately zero in the water column. It can be observed that, except at the discontinuity ($z = -d$), the error is of the order of magnitude of 10^{-2} for the case $B/L = 0.56$ and lower for the rest. The behavior of the solution at the discontinuity, $z = -d$, is due to the Gibbs phenomenon of a truncated Fourier series expansion of a piece-wise function.

5.1.1. Relevance of head loss consideration

The amplification factor Q and the phase lag Ψ were calculated with and without head loss, and compared with the numerical solutions obtained by Teixeira et al. (2013) for different wave periods ($T = 5 - 18$ s) as shown in Figure 5. It can be observed that the analytical model considering head loss ($C_e \neq 0$) presents a similar behavior as the numerical models for both the amplification factor (with mean square errors $R^2 = 0.95$ for Fluent and $R^2 = 0.92$ for Fluinco) and the phase lag (with corresponding values $R^2 = 0.98$ and $R^2 = 0.9$).

The difference in the behavior of the numerical models from the analytical model for $C_e = 0$ reveals the importance of accounting for the head loss. When the analytical model does not consider head loss ($C_e = 0$), there is an amplification ($Q \approx 2.5$) for $B/L = 0.13$, coinciding with a sudden change in the phase lag from 0° to 180°. However, the inclusion of friction eliminates this peak in Q and the results present a more gradual variation of the phase lag.

To illustrate the versatility and the results that can be derived with the proposed analytical model, several kinematic and dynamic properties of interest are investigated for regular and irregular waves.

5.2. Regular Waves

In order to understand the influence of the system's geometry on its behavior, we analyzed the modulus of the reflection and capture coefficients (Equations 16 and 17) for different values of relative submergence d/h and relative width B/L (Figure 6). It can be observed in both figures that the response varies with a periodicity at $B/L = 0.5$.

A maximum value of the modulus of the reflection coefficient ($K_R = 1$) is obtained for the lowest relative submergences ($d/h \lesssim 0.25$), corresponding to the maximum incident wave transmission below the plate and full reflection from the back wall. For values of d/h over 0.25 approximately, the maximum reflection in region 1 (seaward) is obtained for very small values of B/L and for B/L slightly larger than 0.5. In these

cases, maximum values of K_C can also be observed. In general, maximum capture coefficients ($K_C > 1.1$) coincide with higher reflections ($K_R > 0.8$) as observed in Figure 6a. At d/h close to 0.60, the minimum reflection is found at $B/L = 0.1$ and 0.6 (separated $B/L = 0.5$, as in Sahoo et al. (2000)). The efficiency of the system in regard to energy capture is minimum for B/L around 0.3 and 0.8 with bandwidths depending on the relative submergence (Figure 6b).

A similar behavior is observed for oblique wave incidence (Figure 7) with periodicity at $B/L' = 0.5$ where $L' = L/\cos\theta$. As expected, there is a slight variation from the results corresponding to $\theta = 0°$ (also included for comparison in the figure), but the general behavior of the system remains the same. Maximum capture coefficients are obtained for lower values of B/L' and around 0.6 for which a higher reflection is also obtained.

Figure 8 presents the reflection and caption coefficients versus the angle of incidence for $d/h = 0.64$ and different relative widths. The value of the incident angle θ that gives a maximum K_C varies with B/L and seems to reach the best performance for B/L close to 0.6 and $\theta \approx 25°$. For those values, the reflection coefficient is also close to its maximum 1.

Figure 9 presents the values of the maximum dimensionless amplitudes at both sides of the plate, $\max\{\eta_1(x = 0, t)\}/A_0$ and $\max\{\eta_2(x = 0, t)\}/A_0$ in terms of the relative submergence d/h of the plate and the relative width of the chamber B/L.

It can be observed that depending on the phase of the reflection coefficient a variety of values ranging from the amplitudes at quasi-nodes to those at quasi-antinodes are measured at the seaward face of the plate (Figure 9a). Similarly, the relative phase of the transmission coefficient leads to different amplitudes at the leeward side of the plate (Figure 9b).

5.2.1. Peak forces

Values of the phase of the reflection coefficient close to 180° indicate the presence of quasi-nodes in the seaward region ($\max\{\eta_1(x = 0, t)\} \approx 0$) that would therefore generate lower loads acting on the plate towards land (F_l). At the same time, the presence of a quasi-node on the leeward side gives minimum forces on the opposite direction, acting towards sea (F_s). Therefore, these values are decisive factors to obtain the maximum/minimum loads at both sides of the plate; however, the total load on the plate does also depend on the relative phase lag between the surface elevations at both sides presented in Figure 10. To this respect, critical total loads in both directions would be obtained when the surface elevations are approximately in phase opposition ($\Psi \approx 180°$).

Taking into account equations 11c and 20, the time variation of the total force on the plate largely depends on the head loss. Indeed, the larger the difference between the free surface elevations, the larger the absolute value of the force, with a sign depending on the sign of $\eta_1 - \eta_2$. The dimensionless peak forces are presented in Figure 11 defined as the ratio between the peak forces and the maximum force per unit

width exerted by an incident wave train on a wall F_{wall} $(d/h = 1)$ (Dalrymple and Dean, 1991).

As observed, for values around $B/L \approx 0.5$, and despite the maximum reflection and the relatively large amplitudes at the seaward side $\max\{\eta_1(x = 0, t)\}$, forces are in balance due to the fact that the oscillations are almost in phase ($\Psi \approx 0°$) and the most favorable conditions regarding the loads on the plate are obtained ($F_{max} \approx 0$).

In relation to the combination of the maximum/minimum loads on the plate and the capture coefficient inside the chamber, the regions around $0.5 < d/h < 0.7$ and $0.2 < B/L < 0.4$ (with periodicity at $B/L = 0.5$) seem to provide a balance of relatively low forces acting on the plate and low capture coefficients, an ideal situation e.g. for harbor design where lower wave heights are required. On the other hand, when studying the maximum wave energy inside the chamber (i.e. the design of wave energy converters), values around $B/L \approx 0.5$ and $0.3 < d/h < 0.6$ provide an optimum balance of low loads acting on the plate and high capture coefficients.

This behavior shows the importance of a proper design of the chamber regarding its dimensions and geometry accounting for the local wave climate. However, in nature, waves are irregular and the combined action of several frequency components needs to be analyzed.

5.3. Irregular Waves

In the case of irregular waves, the time series of the wave profile and the total wave force acting on the plate are obtained following the methodology presented in section 4. We used a TMA wave spectrum, commonly used in maritime engineering, with a peak wave period $T_p = 7$ s, significant wave height $H_{m_0} = 1.8$ m and peakedness parameter $\gamma = 1$ for the incident wave train. The frequency range was considered so that it includes 90% of the total energy of the incident wave spectrum. The non-dimensionalization of results was done using the peak frequency ($f_p = 1/T_p$), its associated wavelength L_p and the zeroth-order moment (m_0) characteristics of the incident wave spectrum: $H_{m_0} = 4\sqrt{m_0}$ and the value A_{m_0} defined as $A_{m_0} = H_{m_0}/2$.

Figure 12 shows the dimensionless time series of the surface elevation obtained at both sides of the plate for different values of B/L_p and d/h. It can be observed that the presence of the plate, in addition to modify the wave energy content inside the chamber, produces a phase lag between the elevation time series at both sides which follows the same behavoir as in the case of regular waves (Figure 10). The highest surface elevations in the leeward region (η_2/A_{m_0}) are obtained for $B/L_p = 0.5 - 0.6$ as expected by the results of Figure 9b.

In order to understand the behavior of the system's geometry regarding the different wave frequencies present in nature, we analyzed the dimensionless total spectra of the simulated surface elevations in both regions for different values of relative submergence d/h and relative width of the chamber B/L_p (Figure 13). The nondimensionalization corresponds to $S_d = S(f) * f_p/m_0$. The results show a nodal and antinodal frequency structure for the total spectrum in region 2 due to the superposition of the incident and reflected

components. The number of antinodal frequencies and the distance between them vary with the relative width, while the energy for a given B/L_p value varies with the relative submergence.

Figure 14 presents the spectra for the case $B/L_p = 0.6$ and $d/h = 0.64$ at different values of x in the seaward region. It can be observed that the nodal and antinodal structure changes with the distance from the plate. This behavior has to be accounted if for e.g. one of the targets of the design is to obtain the best configuration towards harbor tranquility.

The dynamic loads over the plate also need to be evaluated in order to have an overall picture of the system's performance. This includes the analysis of the forces and moments acting on the structure. In this case, only the forces were analyzed as it is considered a simple way to study the hydrodynamic performance. We analyzed the total force F_t on the protecting barrier as shown in Figure 15 for the same combinations of d/h and B/L_p as previously presented for the surface elevation. The superposition of the loads from both regions, lagged at some frequencies, produces an oscillation of the total force that changes its intensity as well as its direction. Due to the superposition of the incident and reflected components, the leeward surface spectrum presents nodal and antinodal frequencies depending on the geometry of the system.

It can be observed on Figure 15 that the lowest forces are obtained for the case $d/h = 0.24$ in all the considered cases of B/L_p. For higher relative submergences, the cases $B/L_p = 0.3$ and 0.8 present a few higher peaks than $B/L_p = 0.6$ although the general trend remains the same as in the case of regular waves.

The results of the wave forces in combination with the surface elevations are of great interest since these would be the predominant governing variables to study for the design of a wave energy converter device (η amplification) and/or harbor protection (η attenuation) as well as the structural analysis. For example, in the cases of a wave energy converter design, it might be of interest to design a system with $B/L = 0.6$ and $d/h = 0.64$ given that it provides a higher surface elevation amplification and lower forces acting on the plate. This can be observed in Figure 13 in which, for $B/L_p = 0.6$ the amplitude of the oscillations inside the chamber and the energy content at some frequencies is higher than in the seaward region giving, as a result, values of the ratio between forces $F_t/F_{wall} < 1$ in Figure 15.

Figure 16 presents the empirical cumulative distribution function (ECDF) and the Normal distribution fit of the surface elevation in the leeward and seaward regions for $B/L_p = 0.6$ and different values of relative submergence d/h. It can be observed that the CDF of the surface elevation outside the chamber is almost the same regardless of d/h for $x = 0$. However, in the inside it shows a change in variance. Applying the zero-crossing technique to the surface elevation time series, it is possible to obtain the individual wave heights of each signal and their distribution. The wave heights in each region were fitted to Rayleigh distributions. As in the case of the surface elevation, the wave heights in the seaward region present the same distribution regardless of the relative submergence whilst in the leeward region the wave height varies with d/h.

Following the same procedure with the total force time series we obtained the leeward-acting forces F_l (crests) and seaward-acting forces F_s (throughs) and their distributions. Figure 17 presents the ECDF and

the Normal fit of the total forces F_t and the Weibull fit of F_l and F_s. As expected, the case with the lowest relative submergence presents the lowest forces while the cases $d/h = 0.64$ and 0.84 present similar distributions.

6. Example of application

In maritime engineering design, it must be studied if a structure meets the safety requirements in each and every one of the sea states to which it is subjected in the useful life. In general, a sea state is the temporal scale at which the verification equation is formulated for the different failure modes of the structure (ROM 0.0-01, 2001; ROM 1.0-09, 2009; ROM 1.1-18, 2018). The verification equation is formed by the balance between favorable and unfavorable terms and applied considering that, during the sea state, all the parameters and variables remain stationary from a statistical point of view (Solari and Losada, 2014).

Using a safety margin format for the analysis, the verification equation can be written as the difference between favorable and unfavorable terms, $SM = F_c - F_t$ with F_c defined as a critical stress value and failure occurs when $S < 0$.

Simulation techniques were used to obtain the safety margin and to asses its uncertainty. To this end, Monte Carlo techniques were used to generate 100 equally likely 100-wave simulations of surface elevation using the random phase method (Goda, 2010) and the corresponding wave forces time series. This technique relies on repeated random sampling to generate said time series. As presented in section 4, the incident irregular wave train is a superposition of regular wave components. A phase value is randomly drawn from a uniform distribution over $[0, 2\pi]$ to obtain the value of the complex amplitude (Equation 22) of each regular component. Consequently, a large number of equally likely realizations of the irregular wave train can be generated.

Figure 18 presents the results of the simulations by means of the ECDF and theoretical fits of the dimensionless maximum wave heights in the leeward and seaward regions, maximum leeward-acting and seawards-acting forces, and the minimum safety margin for the case of $B/L_p = 0.6$ and $d/h = 0.64$. The probability of failure is defined as the probability that $S < 0$ given that the projected sea-state is exceeded at least once in the timeframe (useful life).

Therefore, this methodology can be used to efficiently project and design maritime studies by means of a simple analytical model and its application with simulation techniques to define the uncertainty of the structure's design.

7. Conclusions

This paper proposes a methodology to analyze the effect of oblique incident regular waves on a maritime structure. The fluid-structure interaction analysis was carried out by developing an analytical model, under

the assumptions of linearized wave theory and taking into account the head loss due to the constriction of the flow. From a practical point of view, as in the case of the model given by Liu and Faraci (2014) for a combined caisson, this analytical model provides a simple and efficient engineering tool for finding the optimal design (trade-off between performance and structural design) towards the goals of (i) controlled wave agitation for harbor tranquility in the seaward region, (ii) energy extraction in the leeward region and (iii) loads acting on the structure.

A simplified configuration was selected for the analysis, however, the model can be easily be extended to a given chamber length (y-axis) by imposing appropriate matching conditions on the borders as well as with an inclined orientation. It could also be extended to an incident directional spectrum to better represent waves in nature as well as an inclined Those simplifications were introduced to avoid the inclusion of extra parameters that would overshadow the presentation of results.

The results of the analytical model were compared to the ones from computational fluid dynamics models (Teixeira et al., 2013). The comparison showed that the proposed analytical model is a simple and efficient tool to analyze the hydrodynamic performance of the structure. Furthermore, the behavior of the system is analyzed through the reflection and capture coefficients and the structural component of the system is dealt by means of the maximum loads acting on the plate.

Finally, Monte Carlo techniques were used to perform a number of equally likely simulations allowing to study the probability of failure and analyze the uncertainty, therefore reducing construction costs.

From an engineering point of view, the more relevant conclusions are:

- Due to the wave-structure interaction, the spectra at both regions contains nodal and antinodal frequencies depending on the geometrical configuration of the system, water depth and the incident wave characteristics (H, T, θ).
- At $x = 0$ the spectrum presents one peak outside the chamber and several peaks inside the chamber. The number of peaks and the distance between them depends on the geometric characteristics. In the seaward region far from the reflector the spectrum presents a nodal structure applicable for controlled harbor agitation.
- This model is an efficient tool for the predesign phase of a maritime structure seeking for an integral optimal configuration regarding:
  - The harbor tranquility in the far field region of the reflector.
  - The structural safety analysis of the loads acting on the plate.
  - Wave energy extraction in the inner chamber.

This study is done by means of the analysis of the reflection coefficient, capture coefficient and forces on the plate under different design and wave characteristics.

- The accurate representation of the phase lag and the general hydrodynamic behavior of the system depends on the correct mathematical representation of the head loss at the gap.
- For increasing wave incidence, the behavior of the system varies with a periodicity at $B/L' = 0.5$ where $L' = L/\cos\theta$.
- Finally, along with Monte Carlo techniques, this model can be used towards the integral optimization of the system (ROM 1.1-18, 2018).

Acknowledgements

This work was performed within the framework of the project AQUACLEW and the research group TEP-209 (Junta de Andalucía). Project AQUACLEW is part of ERA4CS, an ERA-NET initiated by JPI Climate, and funded by FORMAS (SE), DLR (DE), BMWFW (AT), IFD (DK), MINECO (ES), ANR (FR) with co-funding by the European Union (Grant 690462). The first author gratefully acknowledges the CEIBioTic (Spain) for the funding provided for this research.

References

Baquerizo, A., Losada, M., Losada, I., 2002. Edge wave scattering by a coastal structure. Fluid Dynamics Research 31, 275–287.

Bennett, G., McIver, P., Smallman, J., 1992. A mathematical model of a slotted wavescreen breakwater. Coastal Engineering 18, 231–249. doi:10.1016/0378-3839(92)90021-L.

Boccotti, P., 2012. Design of breakwater for conversion of wave energy into electrical energy. Ocean engineering 51, 106–118.

Dalrymple, R., Dean, R., 1991. Water wave mechanics for engineers and scientists. Prentice-Hall.

Dalrymple, R.A., Losada, M.A., Martin, P., 1991. Reflection and transmission from porous structures under oblique wave attack. Journal of Fluid Mechanics 224, 625–644.

Falcão, A.d.O., 2000. The shoreline OWC wave power plant at the azores, in: Proceedings of the Fourth European Wave Energy Conference, Aalborg, Denmark, pp. 42–8.

Faraci, C., Cammaroto, B., Cavallaro, L., Foti, E., 2012. Wave reflection generated by caissons with internal rubble mound of variable slope. Coastal Engineering Proceedings 1, 51.

Faraci, C., Scandura, P., Foti, E., 2015. Reflection of sea waves by combined caissons. Journal of Waterway, Port, Coastal, and Ocean Engineering 141, 04014036. doi:10.1061/(ASCE)WW.1943-5460.0000275.

Goda, Y., 2010. Random seas and design of maritime structures. World scientific.

Huang, Z., Li, Y., Liu, Y., 2011. Hydraulic performance and wave loadings of perforated/slotted coastal structures: a review. Ocean Engineering 38, 1031–1053. doi:10.1016/j.oceaneng.2011.03.002.

Isaacson, M., Baldwin, J., Allyn, N., Cowdell, S., 2000. Wave interactions with perforated breakwater. Journal of waterway, port, coastal, and ocean engineering 126, 229–235.

Isaacson, M., Premasiri, S., Yang, G., 1998. Wave interactions with vertical slotted barrier. Journal of Waterway, Port, Coastal, and Ocean Engineering 124, 118–126.

Jalón, M., Baquerizo, A., Losada, M., 2016. Optimization at different time scales for the design and management of an oscillating water column system. Energy 95, 110–123.

Jarlan, G., 1961. A perforated vertical wall breakwater. The Dock and Harbour Authority 41, 394–398.

Liu, Y., Faraci, C., 2014. Analysis of orthogonal wave reflection by a caisson with open front chamber filled with sloping rubble mound. Coastal Engineering 91, 151–163.

Liu, Y., Li, H.J., 2013. Wave reflection and transmission by porous breakwaters: A new analytical solution. Coastal Engineering 78, 46–52.

Liu, Y., Li, Y., Teng, B., Jiang, J., Ma, B., 2008. Total horizontal and vertical forces of irregular waves on partially perforated caisson breakwaters. Coastal Engineering 55, 537–552.

Liu, Y., Li, Y.c., Teng, B., 2007. The reflection of oblique waves by an infinite number of partially perforated caissons. Ocean engineering 34, 1965–1976.

Losada, I., Losada, M., Baquerizo, A., 1993a. An analytical method to evaluate the efficiency of porous screens as wave dampers. Applied Ocean Research 15, 207–215.

Losada, I., Losada, M., Roldán, A., 1992. Propagation of oblique incident waves past rigid vertical thin barriers. Applied Ocean Research 14, 191–99.

Losada, M.A., Losada, I.J., Roldán, A.J., 1993b. Propagation of oblique incident modulated waves past rigid, vertical thin barriers. Applied ocean research 15, 305–310.

Lovas, S., Mei, C.C., Liu, Y., 2010. Oscillating water column at a coastal corner for wave power extraction. Applied Ocean Research 32, 267–83. doi:10.1016/j.apor.2010.06.004.

Martins-Rivas, H., Mei, C.C., 2009. Wave power extraction from an oscillating water column at the tip of a breakwater. Journal of fluid Mechanics 626, 395–414. doi:10.1017/S002211200900599.

Mei, C., 1989. The Applied Dynamics of Ocean Surface Waves. volume 1. World scientific.

Mei, C., Liu, P., Ippen, A., 1974. Quadratic loss and scattering of long waves. Journal of the Waterways, Harbors and Coastal Engineering Division 100, 217–239.

Mei, C., Stiassnie, M., Yue, D.P., 2005. Theory and Applications of Ocean Surface Waves: Nonlinear Aspects. volume 23. World Scientific.

Monk, K., Zou, Q., Conley, D., 2013. An approximate solution for the wave energy shadow in the lee of an array of overtopping type wave energy converters. Coastal Engineering 73, 115–132.

Mustapa, M., Yaakob, O., Ahmed, Y.M., Rheem, C.K., Koh, K., Adnan, F.A., 2017. Wave energy device and breakwater integration: A review. Renewable and Sustainable Energy Reviews 77, 43–58.

Roldán, A.J., Losada, M.A., Losada, I.J., 1992. Theoretical study of the wave attenuation in a channel with roughened sides, in: Coastal Engineering Conference, American Society OF Civil Engineers. pp. 2786–2786.

ROM 0.0-01, 2001. ROM 0.0. General Procedure and Requirements in the Design of Harbor and Maritime Structures. Puertos del Estado.

ROM 1.0-09, 2009. ROM 1.0. Recommendations for the Project Design and Construction of Breakwaters (Part I: Calculation and Project Factors. Climatic Agents). Puertos del Estado.

ROM 1.1-18, 2018. ROM 1.1. Recomendaciones para el Proyecto de Construcción de Diques de Abrigo. Puertos del Estado.

Sahoo, T., Lee, M., Chwang, A., 2000. Trapping and generation of waves by vertical porous structures. Journal of engineering mechanics 126, 1074–1082.

Sawaragi, T., 1995. Coastal engineering-waves, beaches, wave-structure interactions. volume 78. Elsevier.

Solari, S., Losada, M.A., 2014. Statistical Methods for Risk Assessment of Harbor and Coastal Structures, in: Design Of Coastal Structures And Sea Defenses. World Scientific Publishing Company. Series On Coastal And Ocean Engineering Practice.

Sollitt, C.K., Cross, R.H., 1972. Wave transmission through permeable breakwaters. Coastal Engineering Proceedings 1.

Teixeira, P.R.F., Davyt, D.P., Didier, E., Ramalhais, R., 2013. Numerical simulation of an oscillating water column device using a code based on Navier–Stokes equations. Energy 61, 513–30. doi:10.1016/j.energy.2013.08.062.

Torre-Enciso, Y., Ortubia, I., López de Aguileta, L., Marqués, J., 2009. Mutriku Wave Power Plant: from the thinking out to the reality, in: Proceedings of the 8th European Wave and Tidal Energy Conference, pp. 319–29.

Yu, X., 1995. Diffraction of water waves by porous breakwaters. Journal of waterway, port, coastal, and ocean engineering 121, 275–282.

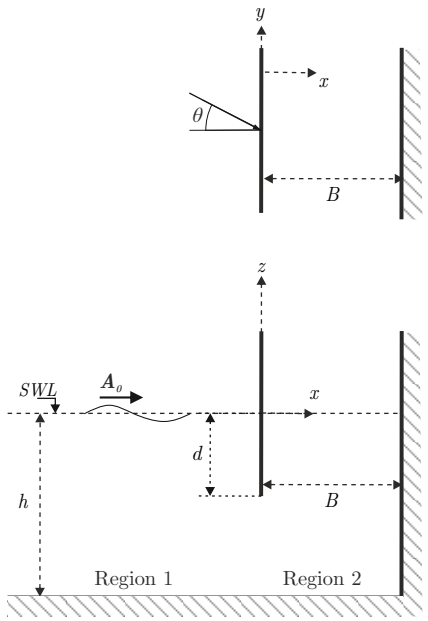

Figure 1: Sketch of the marine structure.

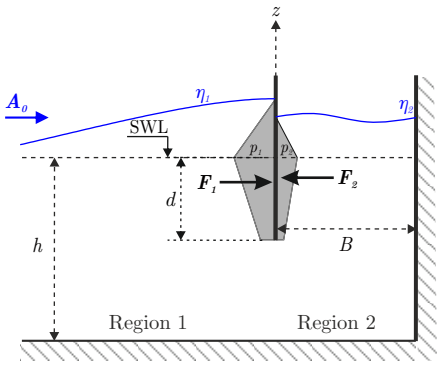

Figure 2: Definition sketch of free surface elevation, pressures and forces on the structure

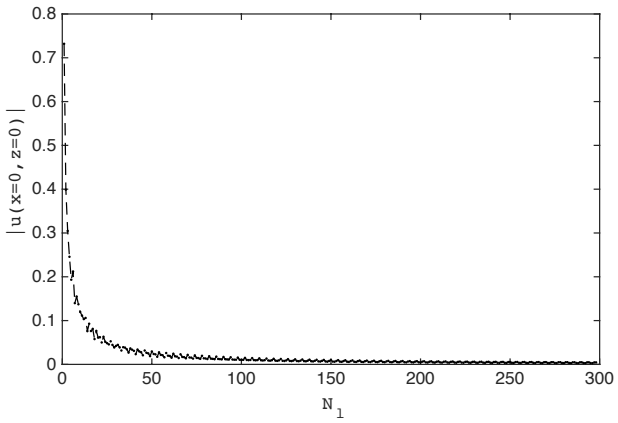

Figure 3: Amplitude of the horizontal velocity component (m/s) in $x = 0$ and $z = 0$, with respect to the number of evanescent modes N_l. $A_0 = 0.5$ m, $\theta = 0°$, $h = 10.0$ m, $kh = 1.717$, $d/h = 0.5$, $B/h = 1$.

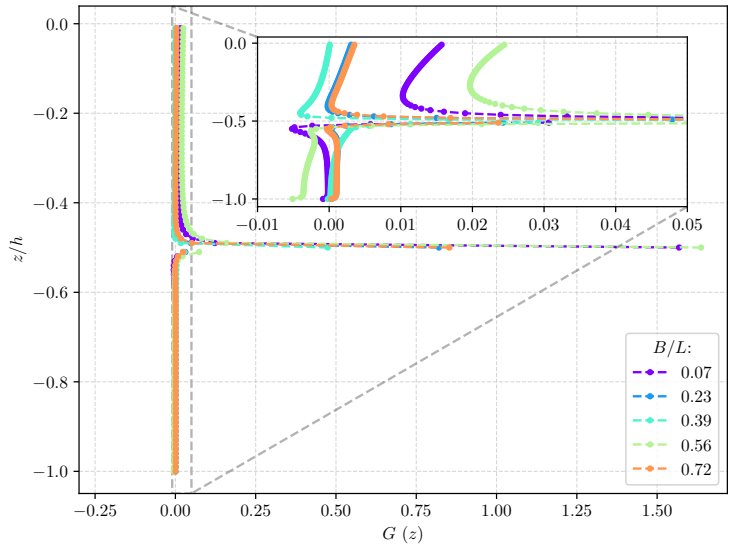

Figure 4: Piece-wise function G(z) for different values of relative width B/L. $A_0 = 0.5$ m, $\theta = 0°$, $h = 10.0$ m, $kh = 1.717$, $d/h = 0.5$, $N_l = 200$.

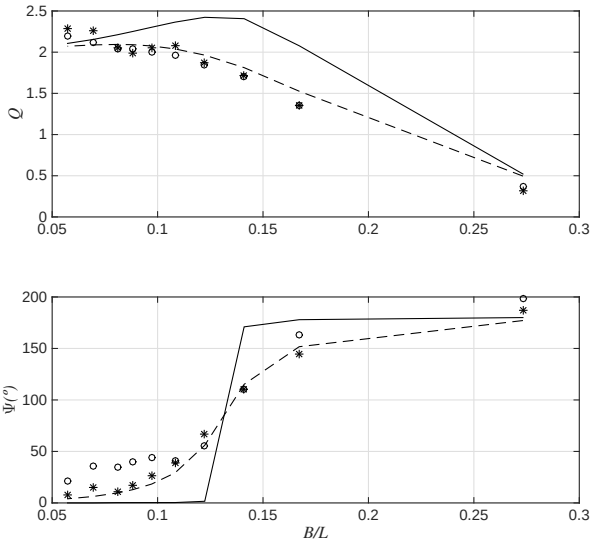

Figure 5: Amplification factor (Q) and phase lag (Ψ) with respect to the relative width B/L. h =10 m, B/h =1, d/h =0.5. Numerical models: Fluent (o), Fluinco (*). Analytical model: $C_e = 0$ (-), $C_e \neq 0$ (- -)

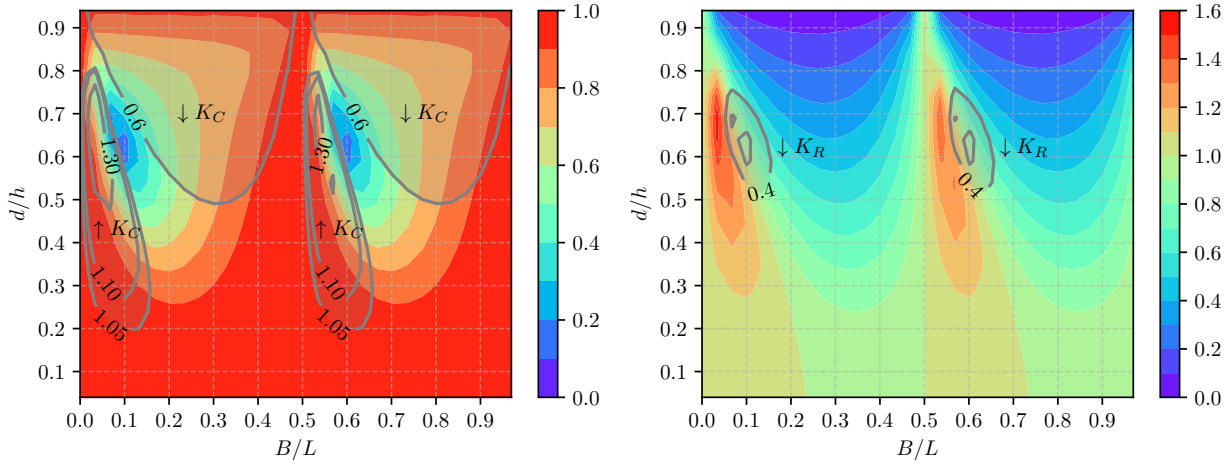

(a) K_R (b) K_C

Figure 6: Modulus of the reflection K_R and capture K_C coefficients with respect to the relative submergence (d/h) and the relative width (B/L) of the system for $\theta = 0°$. Solid lines represent the isolines of (a) the maximum/minimum values of K_C and (b) minimum values of K_R

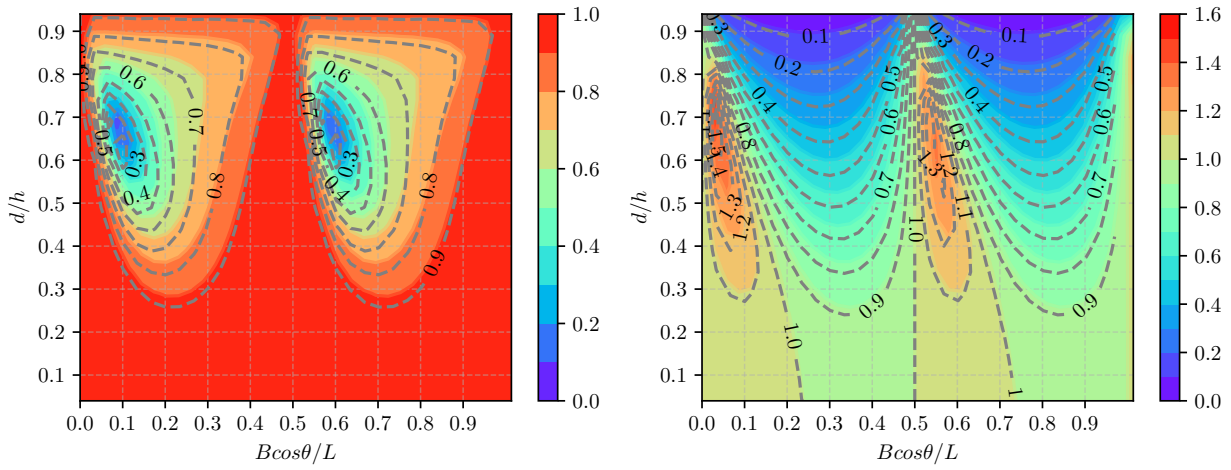

(a) K_R (b) K_C

Figure 7: Modulus of the reflection coefficient K_R and the capture coefficient K_C with respect to the relative submergence (d/h) and the relative width (B/L') of the system with $L' = L/cos\theta$ in the case of oblique incidence. The dashed lines correspond to the contour lines of the case $\theta = 0°$ (Figure 6)

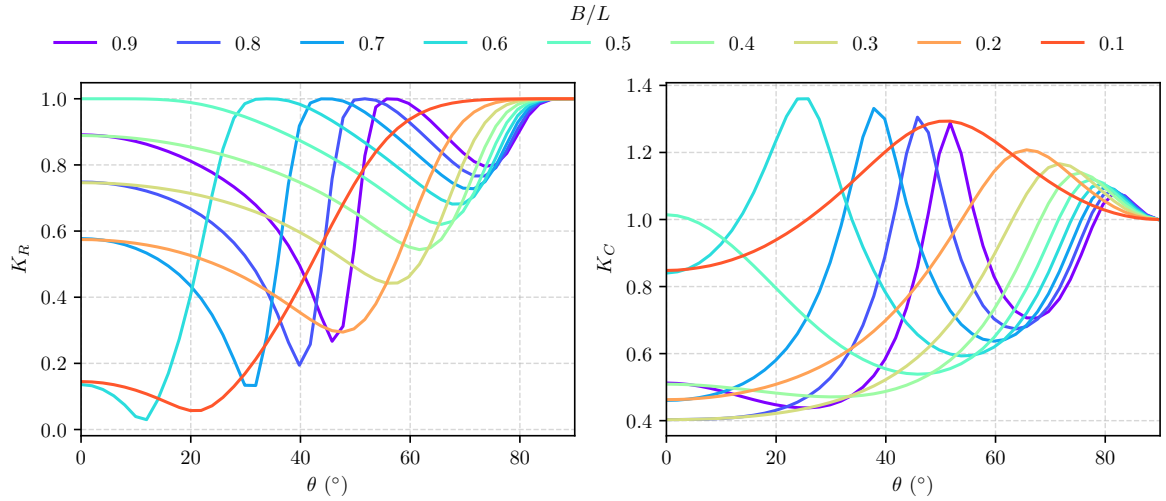

Figure 8: Modulus of the reflection K_R and capture K_C coefficients with respect to the incidence angle (θ) and for different values of relative width (B/L).

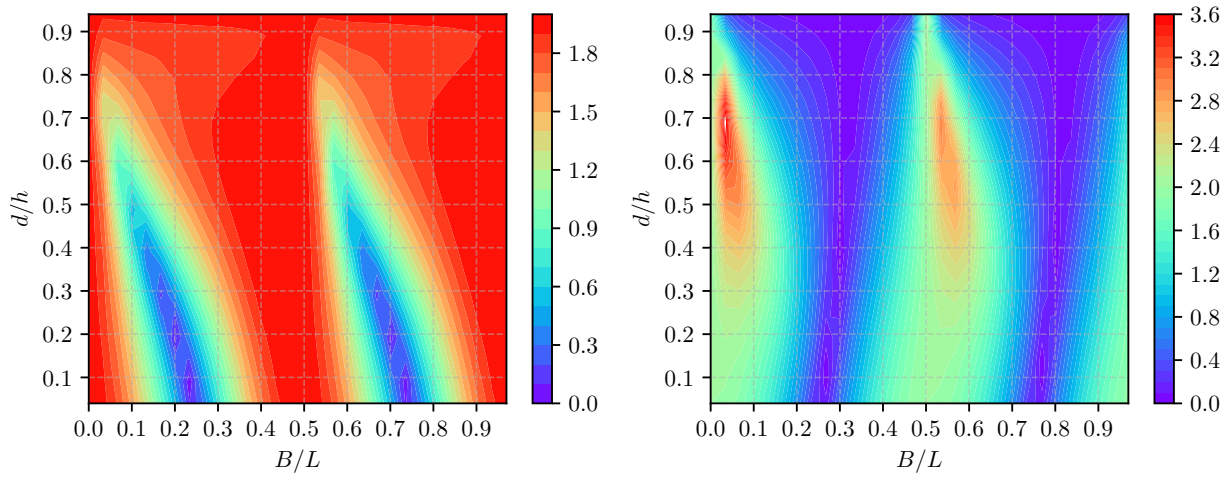

(a) $\max\{\eta_1(x=0,t)\}/A_0$ (b) $\max\{\eta_2(x=0,t)\}/A_0$

Figure 9: Dimensionless amplitude in (a) region 1 and (b) region 2 at $x = 0$ with respect to the relative submergence d/h and the relative width B/L of the system, for the case of $\theta = 0°$

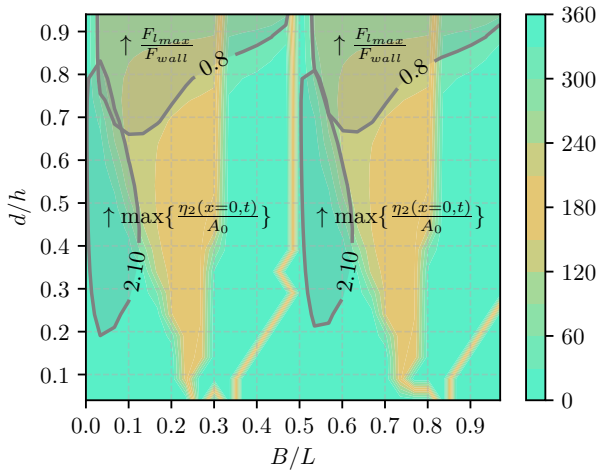

Figure 10: Phase lag (Ψ) between the surface elevation at both sides of the plate with respect to the relative submergence d/h and the relative width B/L. The isolines indicate the areas with the highest values of $\max\{\eta_2(x=0,t)\}/A_0$ (Figure 9b) and $F_{l_{max}}/F_{wall}$ (Figure 11a).

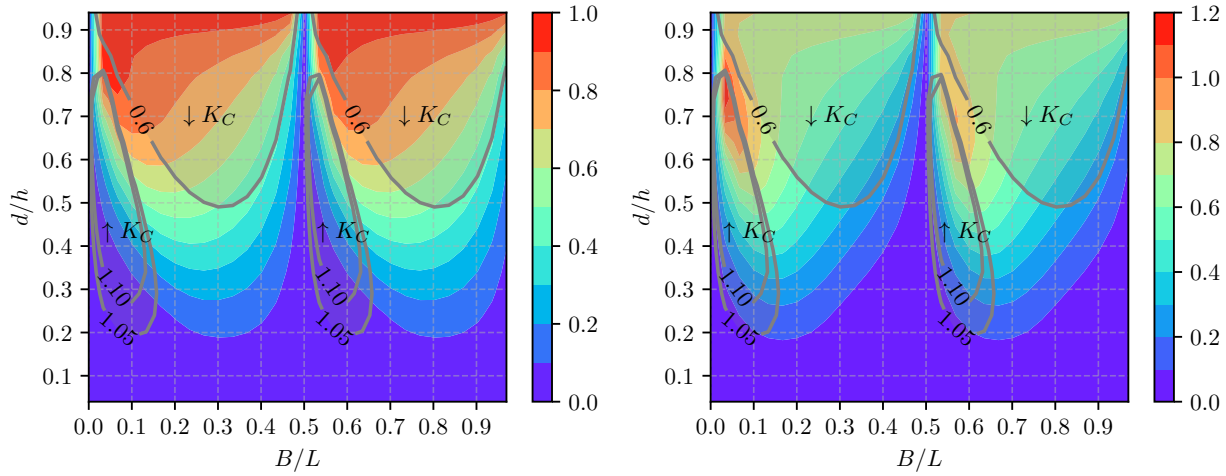

(a) $F_{l_{max}}/F_{wall}$

(b) $F_{s_{max}}/F_{wall}$

Figure 11: Dimensionless leeward-acting peak forces ($F_{l_{max}}/F_{wall}$) and seaward-acting peak forces ($F_{s_{max}}/F_{wall}$) on the plate ($x = 0$) with respect to the relative submergence d/h and the relative width B/L. The solid curves correspond to the isolines around maximum ($\uparrow K_C$) and minimum ($\downarrow K_C$) capture coefficient as estimated in Figure 6b

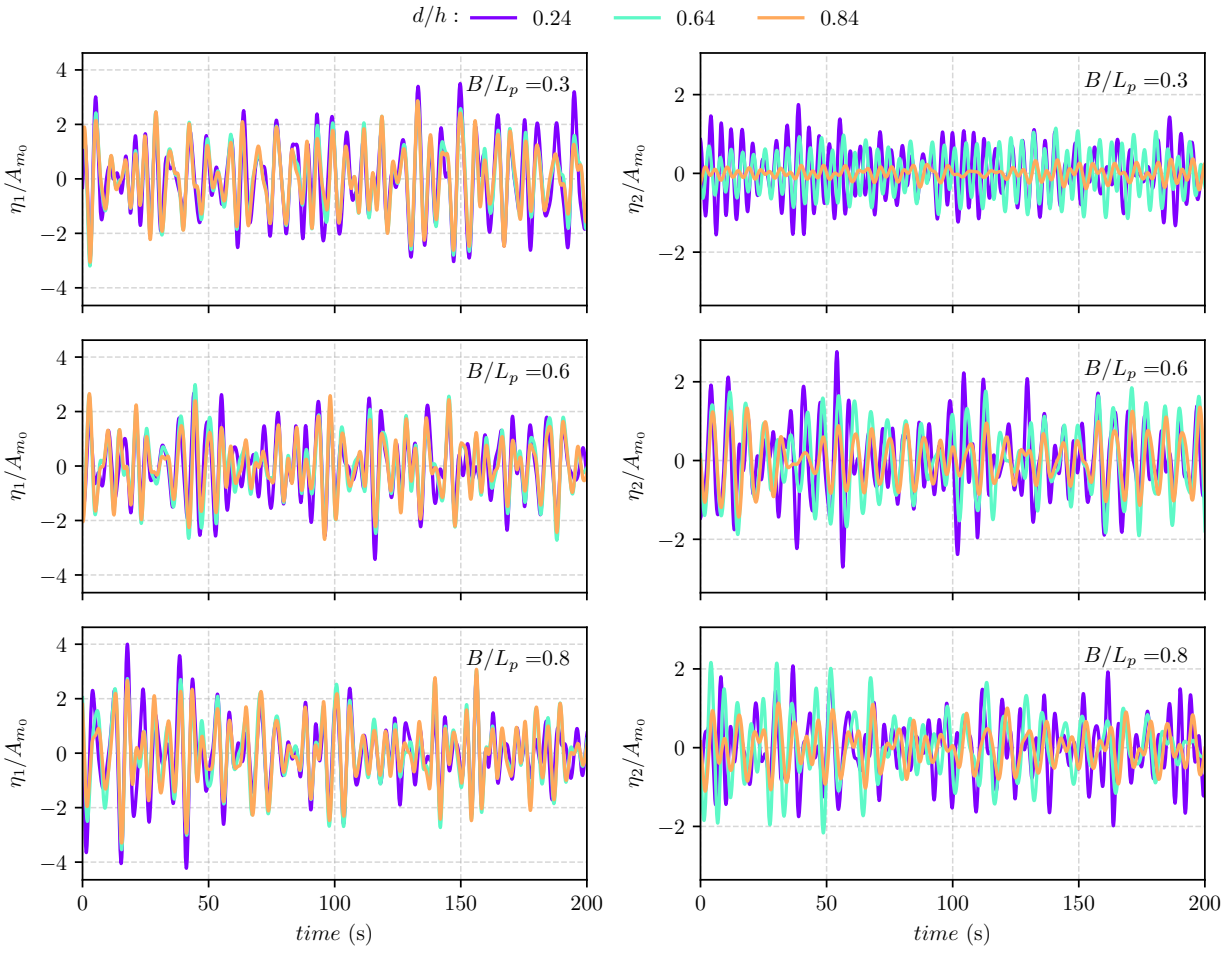

Figure 12: Dimensionless surface elevation time series at $x = 0$ in the seaward (left) and leeward (right) regions for different values of the relative submergence d/h and relative width B/L_p.

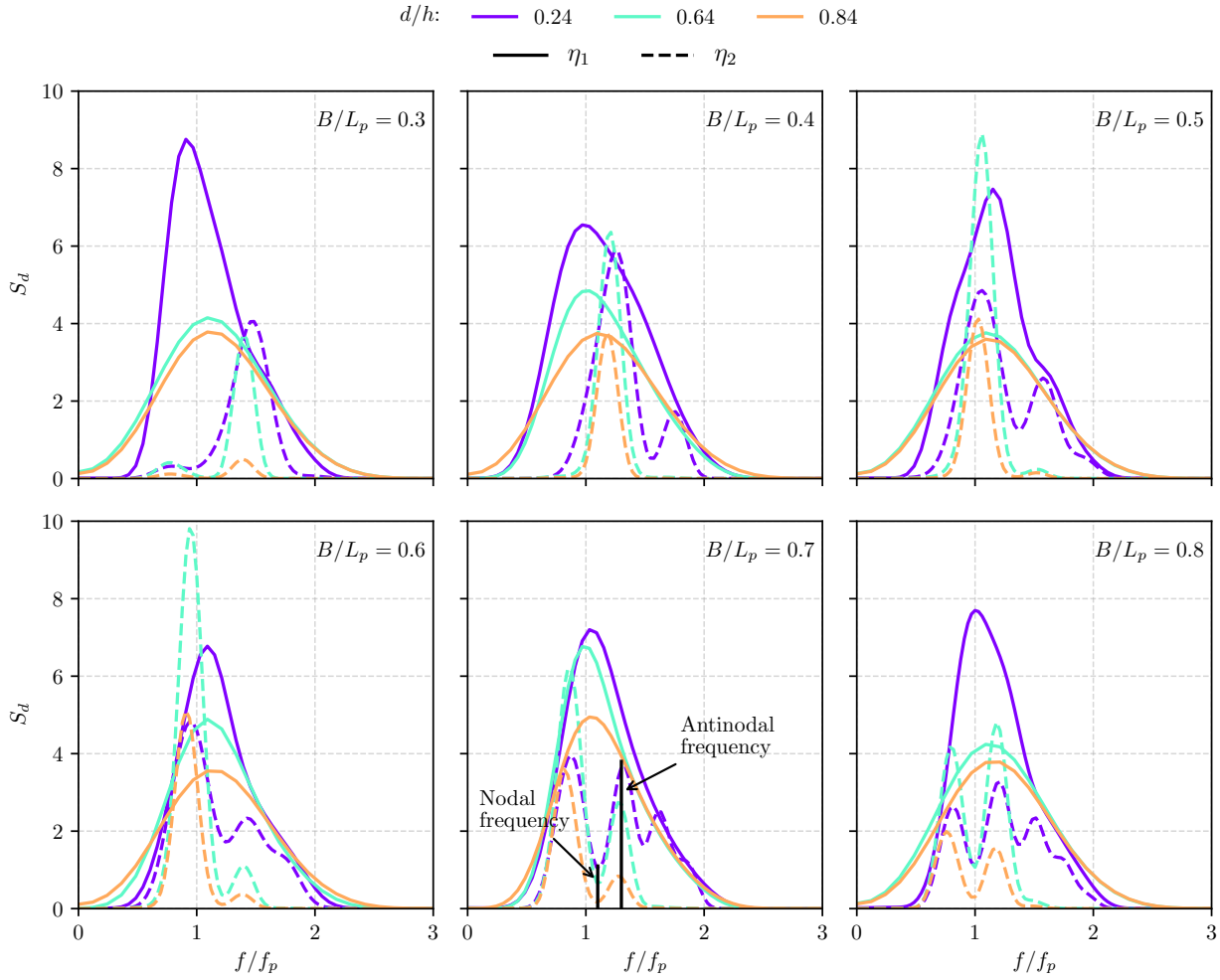

Figure 13: Dimensionless spectrum (S_d) of simulated surface elevation at $x = 0$ in the seaward (solid lines) and leeward (dashed lines) regions for different values of the relative submergence d/h and relative width B/L_p. The location of nodal and antinodal frequencies is illustrated for the case $B/L_p = 0.7$.

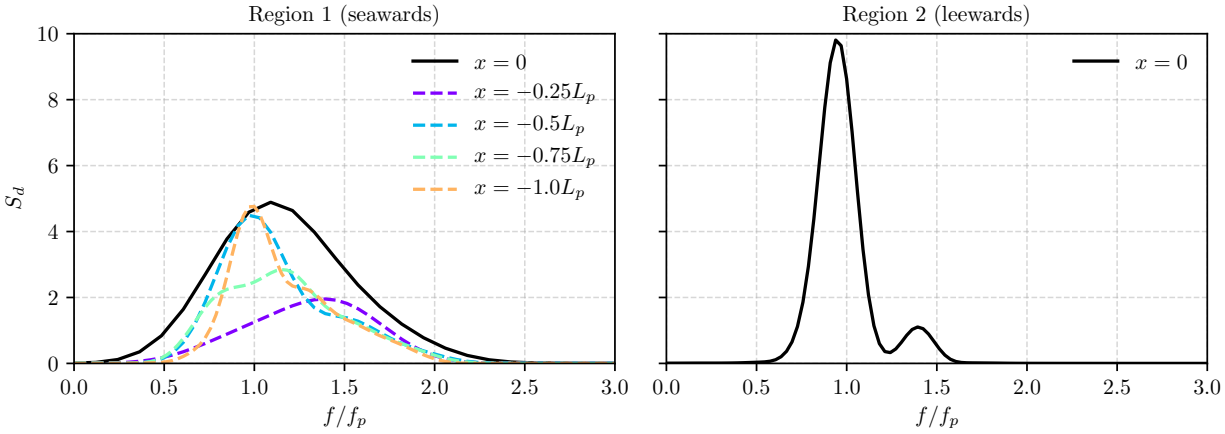

Figure 14: Dimensionless spectrum (S_d) of simulated surface elevation in the seaward region (left) for at different x values and in the leeward region for $x = 0$. These results correspond to the case $B/L_p = 0.6$ and $d/h = 0.64$.

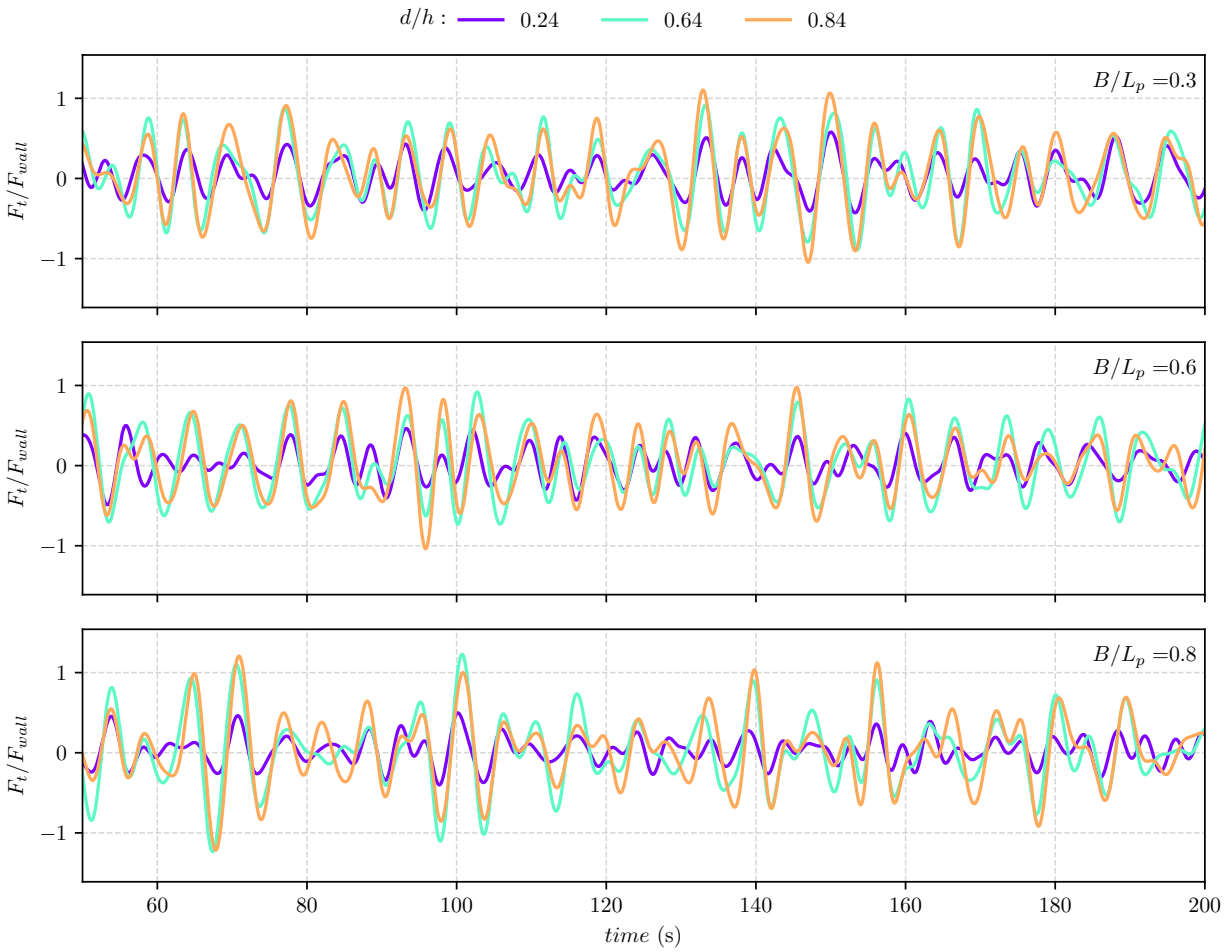

Figure 15: Time series of total wave forces acting on the plate ($x = 0$) for different values of the relative submergence d/h and relative width B/L_p.

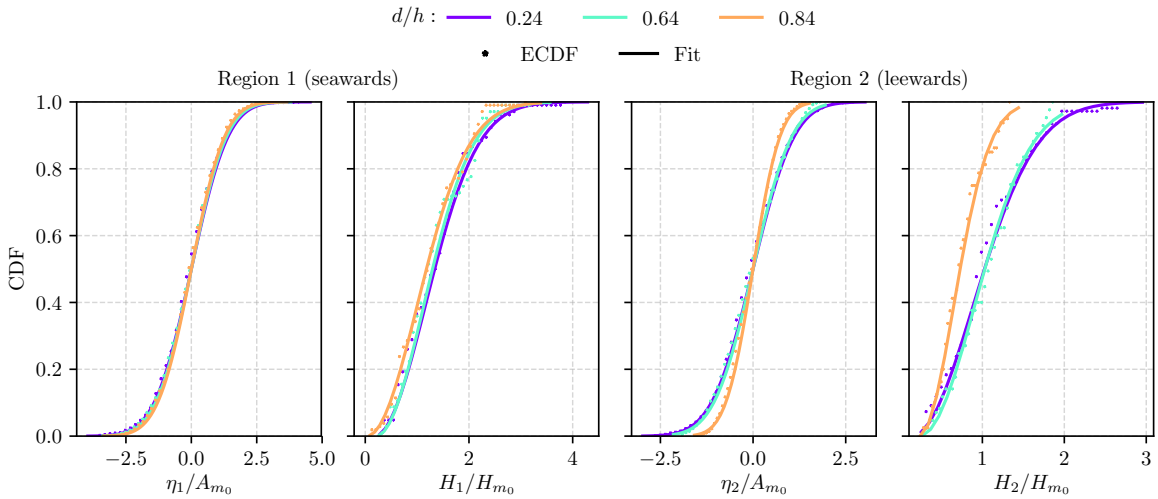

Figure 16: Empirical cumulative distribution function (ECDF) and theoretical fit of the dimensionless surface elevation and wave heights in the leeward and seaward regions at $x = 0$ for $B/L_p = 0.6$ and different values of relative submergence d/h.

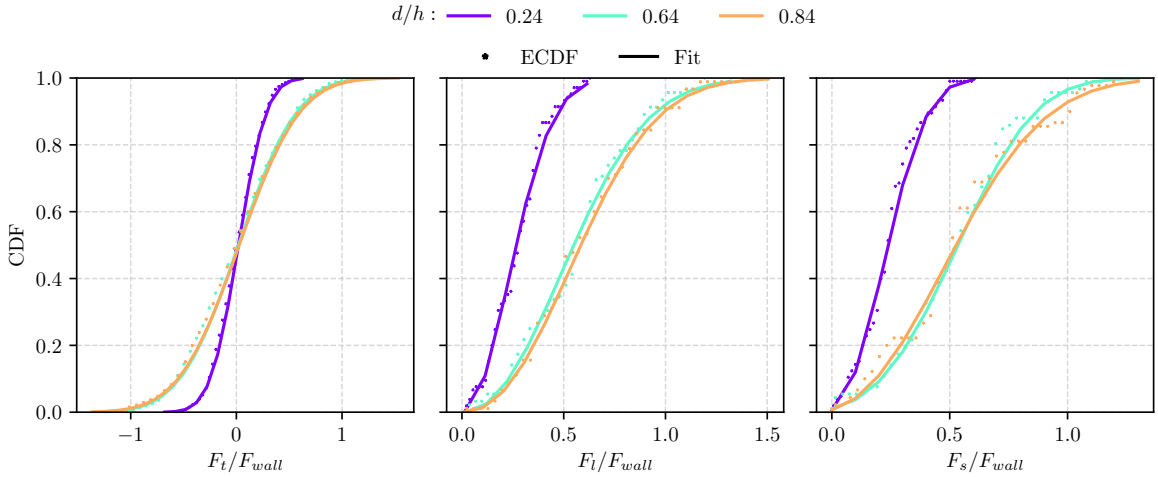

Figure 17: Empirical Cumulative Distribution Function (ECDF) and theoretical fit of the dimensionless total force F_t (left), leeward-acting forces F_l (middle) and seaward-acting forces F_s (right) on the plate ($x = 0$) for $B/L_p = 0.6$ and different values of relative submergence d/h.

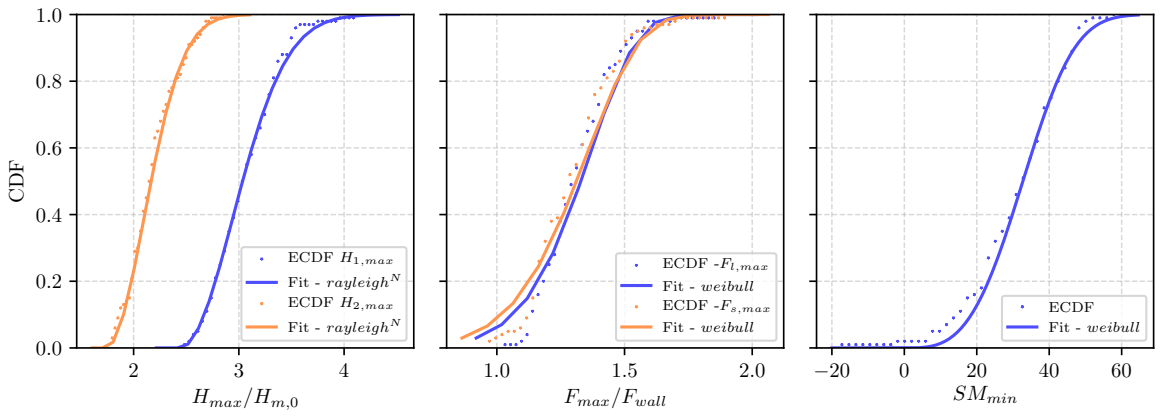

Figure 18: Empirical Cumulative Distribution Function (CDF) and fit of maximum wave height inside and outside the chamber (left), maximum total forces (middle) and minimum safety margin (right) at the plate ($x = 0$) for different $B/L_p = 0.6$ and $d/h = 0.64$.